TECHNISCHE UNIVERSITÄT WIEN

Masterarbeit

Enhancing the High Field Performance of $YBa_2Cu_3O_{7-x}$ Coated Conductors

Ausgeführt am

Atominstitut, TU Wien

und am

Argonne National Laboratory, Lemont, Illinois, USA

unter der Anleitung von

Priv.Doz.Dipl.-Ing.Dr.techn. Michael Eisterer

und

Dr. Wai-Kwong Kwok

Dr. Ulrich Welp

durch

Sigrid Holleis

Bräuhausgasse 64/18

A-1050 Wien

Wien, am 2. Mai, 2016

Sigrid Holleis

Enhancing the High Field Performance of $YBa_2Cu_3O_{7-x}$ Coated Conductors

Masterarbeit Technische Physik
Technische Universität Wien

Weitere Betreuer: Karen J. Kihlstrom, Maxime Leroux

Bearbeitungszeitraum: 20. April 2015 - 20. November 2015

Acknowledgments

The experiments for this thesis were conducted while working with the Superconductivity and Magnetism Group at the Materials Science Division at Argonne National Laboratory in Lemont, Illinois, USA.

I would like to thank my adviser Michael Eisterer, who was incredibly supportive from the moment I expressed the wish to work at an institution abroad and who constantly continues to support my scientific career. Thanks also to all my colleagues at the ATI Wien for our good times together while I was writing this thesis.

I want to express my gratitude to Wai-Kwong Kwok for giving me the exciting opportunity to work in his group and to Ulrich Welp for constantly giving me scientific input during my stay. I also want to thank Maxime Leroux for our work together, Andreas Glatz for giving me a roof over my head and all the other colleagues at ANL that made my stay such a wonderful experience. I especially want to thank Marlene Metz for helping me in all organizational matters and for being such a good friend. My biggest thanks goes to Karen Kihlstrom, who accompanied me through all experiments and who shared so much of her knowledge with me. Thank you for being such a great lab partner and friend.

Finally, I would like to thank my parents for their financial support throughout my studies and my family for encouraging me to always follow my dreams.

This work was supported by the KUWI Program TU Wien, by a TOP Stipendium Niederösterreich and by UChicago Argonne LLC.

Abstract

The in-field critical current of commercial $YBa_2Cu_3O_{7-x}$ (YBCO) coated conductors can be substantially enhanced by post-fabrication irradiation with $^{16}O^{3+}$ oxygen ions. We find that the maximum enhancement of J_c can be observed when choosing an irradiation energy of 3.5 MeV on the YBCO surface. In high fields of 6 T, J_c is doubled at 5 K and 27 K after irradiating the sample for only one second. The irradiation is performed on production line samples through the protective silver coating and does not require any modification of the growth process. TEM images reveal a mixed pinning landscape composed of strong pre-existing pin sites and small, finely dispersed irradiation induced defects. These irradiation induced defects can be identified as the main source of increased vortex pinning. An annealing study shows that the enhancement is stable up to approximately 200 °C for over an hour and the irradiated conductor would therefore survive a possible quench.

Zusammenfassung

Die kritische Stromdichte von hochtemperatursupraleitenden $YBa_2Cu_3O_{7-x}$ (YBCO) Bändern kann durch Bestrahlung mit $^{16}O^{3+}$ Sauerstoffionen erheblich gesteigert werden. Dabei wird die maximale Verbesserung von J_c bei einer Bestrahlungsenergie von 3.5 MeV an der YBCO Oberfläche beobachtet. Bei hohen angelegten magnetischen Feldern von bis zu 6 T wird eine Verdopplung von J_c bei Temperaturen von 5 K und 27 K nach nur einer Sekunde Bestrahlungszeit erreicht. Die Bestrahlung erfolgt durch die Silber-Schutzschicht an produktionsfertigen supraleitenden Bändern, sodass keine Änderung am Wachstumsprozess notwenig ist. TEM Bilder zeigen eine kombinierte Verankerungsstruktur aus starken, bereits existierenden Verankerungszentren und kleinen, feinverteilten Bestrahlungsdefekten, wobei letztere als Hauptursache der verstärkten Flussverankerung identifiziert werden können. Experimente in einem Röhrenofen zeigen, dass die Verbesserung von J_c bis zu einer Temperatur von 200 °C über eine Stunde stabil ist und der bestrahlte Leiter einen denkbaren Quench unbeschadet überstehen würde.

Contents

Chapter 1

Introduction

Superconductivity is a thermodynamic state which occurs in certain materials at low temperatures. In 1911 Kammerlingh Onnes discovered that the resistance of Hg dropped to zero at a temperature of 4.19 K. Soon after the discovery of this new state called superconductivity it was found that superconductivity is not only destroyed by heating the sample above a certain temperature, the critical temperature T_c, but is also limited by a certain magnetic field, the critical field H_c. Meissner and Ochsenfeld found in 1933 that when a superconductor is cooled below T_c in a weak magnetic field $H < H_c$, the field is expelled from the superconductor. This complete field expulsion, called the Meissner effect, is a fundamental property of superconductivity. Another important characteristic is the maximum possible transport current which can flow without dissipation, or more commonly used, the critical current density J_c. In 1952 Abrikosov classified superconductors into two kinds according to their behavior in external magnetic fields: type I and type II superconductors. The first are mostly pure elements which have a low critical temperature and magnetic fields $H < H_c$ are completely screened due to the Meissner effect. The samples used for the experiments in this thesis are type II superconductors which behave differently in magnetic fields and will be treated in more detail in the following chapters.

1.1 Vortex Pinning

In 1937 Shubnikov was the first to suggest the fundamental nature of type II superconductivity. He found that a sample in an external magnetic field does not show total flux expulsion except for very low fields. Type II superconductors are therefore defined by a lower and upper critical field, H_{c1} and H_{c2}, respectively. Figure 1.1 shows the H-T diagram of a typical ideal type II superconductor.

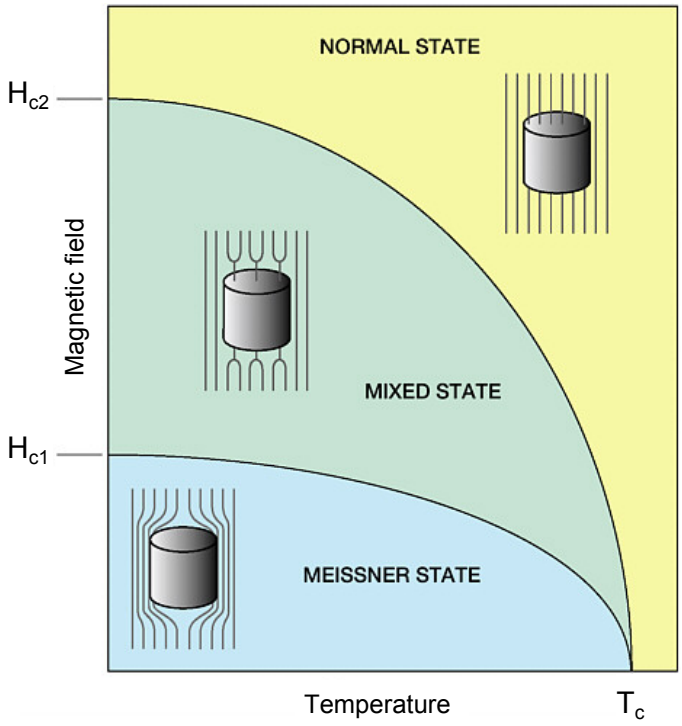

Figure 1.1: Phase diagram of a typical type II superconductor, adapted from [1].

For weak fields $H < H_{c1}$ all flux is expelled, similar to type I superconductors, which is therefore called the Meissner phase. For $H > H_{c1}$ the magnetic field penetrates the superconductor in form of superconducting vortices, where each vortex carries a magnetic flux equal to a superconducting flux quantum

$$\Phi_0 = \frac{h}{2e} \approx 2.07 \cdot 10^{-15} \text{ Wb} \tag{1.1}$$

with Planck's constant $h = 6.626 \cdot 10^{-34}$ J s and the charge of an electron $e = 1.602 \cdot 10^{-19}$ C. Complete penetration of magnetic flux happens at the

upper critical field H_{c2} and the sample becomes normal conducting at higher fields. In the field range $H_{c1} < H < H_{c2}$ the superconductor is in the mixed state, also called the Shubnikov phase. Abrikosov described this mixed state as a vortex state that results from the penetration of magnetic vortices into the superconductor. In equilibrium conditions the vortices form a regular vortex lattice (Abrikosov lattice). If there is a net current of density J flowing in the superconductor then a Lorentz force $\vec{F_L} = \vec{J} \times \vec{B}$ acts on the flux lines which causes the flux lines to move in an ideal type II superconductor. The local magnetic field changes and therefore generates an electric field which acts on the normal conducting vortex core. This causes a resistance and therefore energy dissipation.

Real type II superconductors have defects, such as nanoparticles, dislocations and planar defects which act as pinning centers for vortices and therefore keep the flux lines from moving. The vortices are pinned to these defects by a pinning force F_P as long as the Lorentz force acting on the vortices is smaller. At the critical current density J_c the pinning force and Lorentz force cancel each other out. At higher currents the Lorentz force takes over and vortices start moving again, causing a resistance. The concept of so-called vortex pinning in type II superconductors is important for large-scale applications such as manufacturing high-performance superconducting wires and high-field magnets. The practical goal of material engineering is to create as many pinning centers as possible to prevent the vortices from moving freely and thus to enable high critical currents in high magnetic fields.

1.2 Bean's Critical State Model

In 1962 Bean published his theory of magnetization hysteresis after intensive studies on magnetization curves of type II superconductors [2–4]. He assumed a critical current density J_c that depends on the material but is independent of magnetic field. This is a very good approximation at high fields where the external field is much larger than the self-field so that the field across the superconductor doesn't vary much. The model states that there are only three different values for the current density inside a superconductor, namely $J = 0$ and $J = \pm J_c$. Figure 1.2 (a) shows a cross-section of a superconducting sample

and the resulting magnetic profile inside the sample for increasing external field. The magnetic induction inside the sample shows a linear decrease and once H^* has been reached magnetic flux penetrates the center of the sample. Figure 1.2 (b) shows the corresponding current density distribution inside the sample. Increasing the external magnetic field beyond H^* merely shifts the magnetic profile upwards while $J_c = const.$ In case of a reversal of the external magnetic field by a total of $2H^*$, the magnetic profile and the current density inside the sample are also completely reversed.

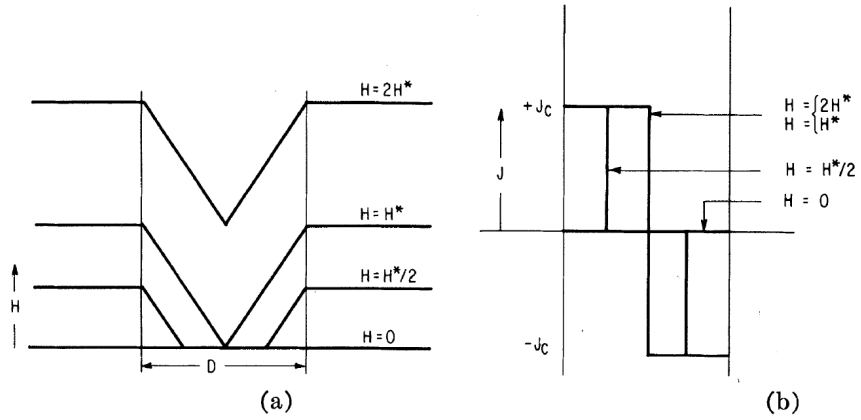

Figure 1.2: Magnetic profile at increasing external field (a) and corresponding current density (b) according to the Bean model [3].

The Bean model can therefore be used to calculate J_c for a known magnetic moment m. For a superconducting sample with dimensions a, b and c and a volume of $V = abc$ the following equation [5] gives the relation

$$J_c = \frac{4 \mid m_{irr} \mid}{Vb(1 - \frac{b}{3a})}, a > b \tag{1.2}$$

where $\mid m_{irr} \mid$ is the irreversible magnetic moment resulting from the current density profile inside the sample. The Bean model is a simple yet useful explanation of flux penetrating type II superconductors and is commonly used for the calculation of J_c from magnetization measurements.

1.3 Motivation

There are many potential applications for superconducting tapes based on $YBa_2Cu_3O_{7-x}$ films coated onto metallic substrates [6]. Increasing the current carrying capacity of second generation YBCO high temperature superconducting (HTS) wires in the presence of high magnetic fields is critical for the commercialization of HTS based rotating machine applications such as wind turbines and motors as well as various magnet applications [7, 8]. Here, the rapid suppression of the critical current density J_c in even modest applied magnetic fields is still a major challenge for HTS conductor development.

One way to increase the critical current density besides modifying the chemical synthesis is given through particle irradiation. Depending on the mass and energy of the ions and the properties of the superconducting material, irradiation enables the creation of defects with well-controlled density and topology such as points, clusters, or tracks. Their effect on vortex pinning in superconductors like HTS single crystals [9–12] and Fe-based superconductors [13, 14] has been well studied. However, their potential for improving the performance of commercial coated conductors has only recently been explored [15, 16].

Especially, in their previous work [16], the Superconductivity and Magnetism group at the Materials Science Division at Argonne National Laboratory has demonstrated that the in-field critical current density of short samples cut from production-line coated conductors can be doubled using irradiation with 4 MeV protons. It is believed that the mixed pinning landscapes that come from the superposition of pre-existing defect structures and $\sim$5 nm sized irradiation-induced defects are particularly efficient for vortex pinning in high fields.

The excellent results using proton irradiation has led to the search of irradiation possibilities with bigger particles and the pursuit to reduce irradiation time. Simulations using the SRIM-TRIM software package [17] show that for irradiation with 6 MeV oxygen ions the peak of maximum damage occurs in the substrate, see Fig. 1.3. Using 6 MeV oxygen ion irradiation the team at Argonne was able to get similar enhancement results as for 4 MeV proton irradiation while reducing the exposure time to approximately one minute. Further simulations indicate that irradiation with 3.5 MeV oxygen ions creates approximately 10^4 times more displacements per incident particle than

the comparable 4 MeV proton irradiation mentioned above, implying a significant reduction in irradiation time. Figure 1.3 shows the damage profile created in the tape by oxygen ions for different energies. Most of the damage occurs within a few microns below the surface, in a limited range of depth at the end of the ions flight path. A 3.5 MeV oxygen beam positions the Bragg peak inside the YBCO layer, thus increasing the defect creation in the middle of the YBCO layer 5-fold as compared to a 6.0 MeV oxygen beam. However, irradiation at 3.5 MeV creates a slightly less uniform damage profile throughout the YBCO layer. These estimates account for the energy loss of the ions in the silver cover layer.

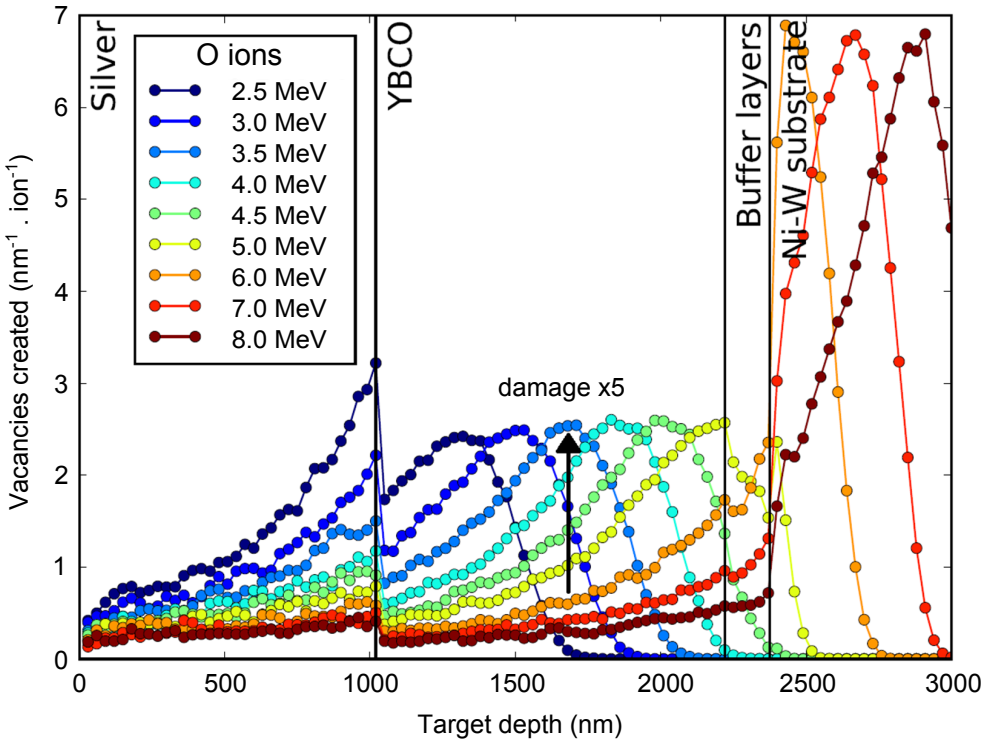

Figure 1.3: SRIM-TRIM simulations showing the number of vacancies created by oxygen irradiation in the YBCO tape layers [18]. For higher incident beam energies the peak of maximum damage occurs deeper in the material. At 6.0 MeV the peak occurs in the substrate and only the tail contributes to creating defects in the YBCO layer. However, at 3.5 MeV the peak is in the YBCO layer thus enhancing the damage creation rate by a factor of 5 in the middle of the layer.

The goal of the experiments conducted for this thesis was to cut down the irradiation time to a few seconds in order to make this method attractive for viable high-speed processing. The samples that were used and all experimental methods and results will be discussed in the following chapters.

Chapter 2

Samples and Methods

This chapter gives an overview of the YBCO coated conductors that were used and how samples for further measurements were prepared and treated at the Center for Nanoscale Materials at Argonne National Laboratory. Furthermore the process of oxygen ion irradiation at the accelerator facility at Western Michigan University is discussed. Before the actual irradiation process of samples several preparations like Rutherford Backscattering to determine the thickness of the silver coating and equilibrium charge state distribution measurements are necessary.

2.1 Sample Preparation

The samples were obtained from production line Dy-doped $YBa_2Cu_3O_{7-x}$ coated conductors manufactured by American Superconductor Corp (AMSC). The superconducting films were deposited onto a Rolling Assisted Bi-axially Textured Substrate (RABiTS) using Metal-organic Deposition (MOD) [19]. The current MOD growth process produces a uniform defect structure in the YBCO superconductor layer consisting of a dispersion of rare earth oxide nanoparticles, stacking faults, twin boundaries and dislocations [20]. Between the YBCO layer and the substrate are several buffer layers and on top of the superconductor layer is a silver coating for protection, as can be seen in Fig. 2.1.

Several sample strips, 50 mm long and 11 mm wide, were cut from both ends of standard 46 mm wide production strips. From these sample strips we can

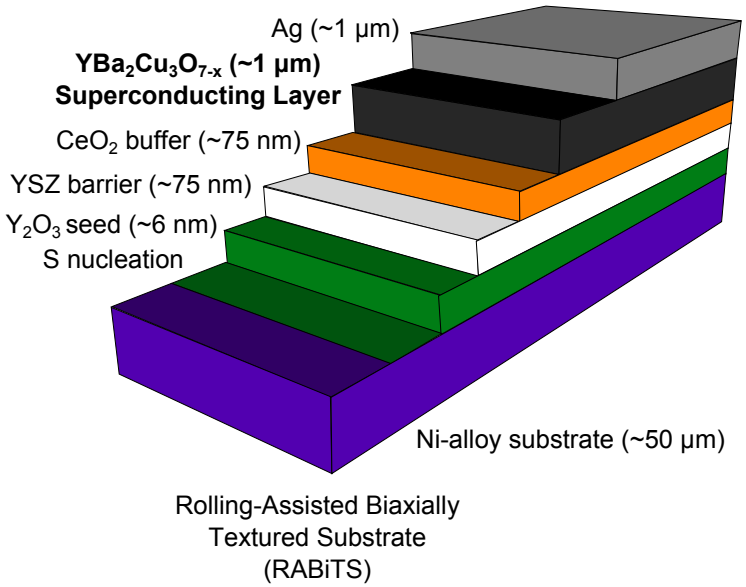

Figure 2.1: Schematic of the different layers of the standard production line tape. Between the YBCO superconducting layer and the Ni-W substrate are several buffer layers and on top is a silver coating for protection.

obtain small 1.5 mm x 1.5 mm square samples from photolithography and Ar-ion milling in the Center for Nanoscale Materials (CNM) at Argonne National Laboratory.

In order to distinguish the silver coated side with the superconductor underneath from the substrate we used a strong oxidizer to etch off the silver. We prepared a solution of

Hydrogen peroxide	:	Ammonium hydroxide	:	Water
1	:	1	:	2

where the first is the oxidizer and put in one end of a sample strip for approximately 30 seconds. On one side of the sample the silver is etched off and the black YBCO layer becomes visible. With the certainty of the right sample side, an approximately 1 cm long piece is cut off and taped onto a silicon substrate with the silver side facing up. The sample is then placed onto a spin coater and the vacuum is turned on to hold the sample in place. We use a positive photo resist (Shipley 1827) with a final thickness of 2.7 μm to cover

the whole sample and spin it at 3000 rpm for 40 seconds. In order to soft bake the sample, it is then placed on a hot plate at 115 ℃ for 60 seconds.

Next, the sample is placed in the laser writer (LW405, Microtech), where a pattern for twelve 1.5 mm x 1.5 mm samples is chosen. Once the lens is set in place, the chosen program moves the sample stage horizontally while the sample is exposed to the laser strip by strip, leaving out the chosen pattern of twelve squares. Since we used a positive photo resist, the surface that is exposed to the laser will be removed. Once the pattern has finished, the sample is developed in a solution of one part developer 351 and two parts water for approximately 60 seconds. After that it is possible to see the silver surface with twelve little squares covered by photo resist. The silver is then etched off with the oxidizer described above while the photo resist protects the sample squares.

Finally the sample is placed in an Ar-ion mill, where the rest of the YBCO layer is removed by Argon ions within approximately 70 minutes. During that time, the photo resist still protects the square samples while the rest of YBCO is removed. The sample strip can now be cut into twelve separate samples where each is put in a sample box and named ANL-286-A1 -#(1-12).

2.2 Oxygen Ion Irradiation

The irradiation of samples was conducted at the 6.0 MV tandem Van de Graaff accelerator at the Western Michigan University in Kalamazoo, Michigan. The samples were irradiated with $^{16}O^{3+}$ ion beams along the normal of the film plane (c-axis). The following sections describe the irradiation process and necessary preparations.

2.2.1 Determination of Silver Thickness through Rutherford Backscattering

The sample strips obtained from AMSC are supposed to have a silver thickness of 1 μm. Since the silver thickness, amongst other parameters, determines the incident beam energy for the sample irradiation it is advisable to confirm the

thickness through Rutherford Backscattering (RBS). In order to obtain a clear signal we use a relatively big sample of approximately 1 cm^2. The incident proton beam is chosen with an energy of 2 MeV and a current of 80 nA. The proton beam is guided into the sample chamber and hits the sample surface, as shown in Fig. 2.2. As the protons hit the target they are scattered in all possible directions inside the chamber. All protons that are elastically backscattered at a precise angle of 150° are detected.

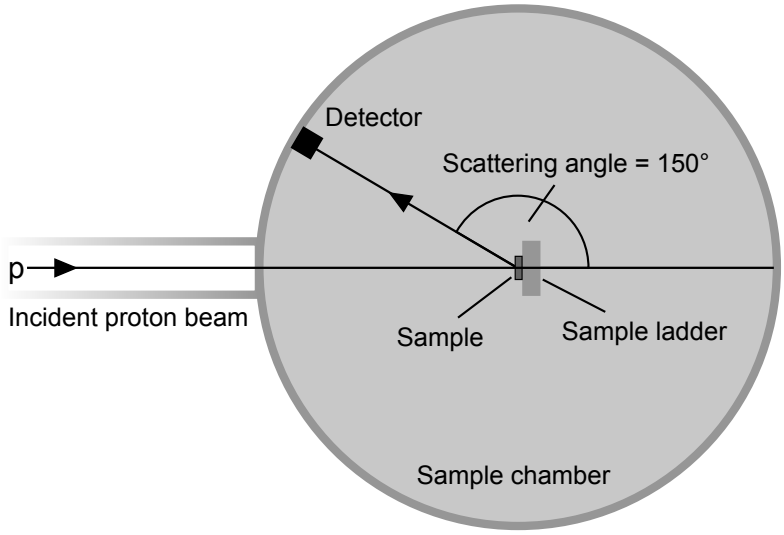

Figure 2.2: Schematic experimental setup for Rutherford Backscattering. The proton beam which hits the target inside the sample chamber is scattered in all possible directions. A detector at a scattering angle of 150° detects all the protons that are elastically backscattered at that precise angle.

In order to get good statistics we let the detector count for several minutes. SIMNRA simulations [21] find the different energy contributions of the sample layers where we can find N, the detected silver atoms per cm^2. From that the thickness d of the silver layer can be calculated with

$$N \cdot A = N_A \cdot \rho \cdot \frac{A \cdot d}{m} \tag{2.1}$$

$$d = N \cdot \frac{m}{N_A \cdot \rho} \tag{2.2}$$

where $\rho = 10.49$ g/cm^3 and $m = 107.87$ g/mole are the density and molar mass of silver and $N_A = 6.022 \cdot 10^{23}$ atoms/mole is Avogadro's constant. We find $N = 6300 \cdot 10^{15}$ silver atoms/cm^2 which determines the thickness of the silver layer to be $d = 1.07$ μm and thus confirming the value obtained by AMSC.

2.2.2 Determination of the Average Charge State

For our oxygen ion irradiation of samples we use a gold foil with carbon backing in order to spread the incident accelerator beam and obtain a uniform beam spot. As the O^{3+} ions go through the gold foil they change their charge through interaction with the Au atoms. Therefore it is necessary to measure the equilibrium charge state of the beam after going through the gold foil. A schematic for the experimental setup for this measurement is given in Fig. 2.3.

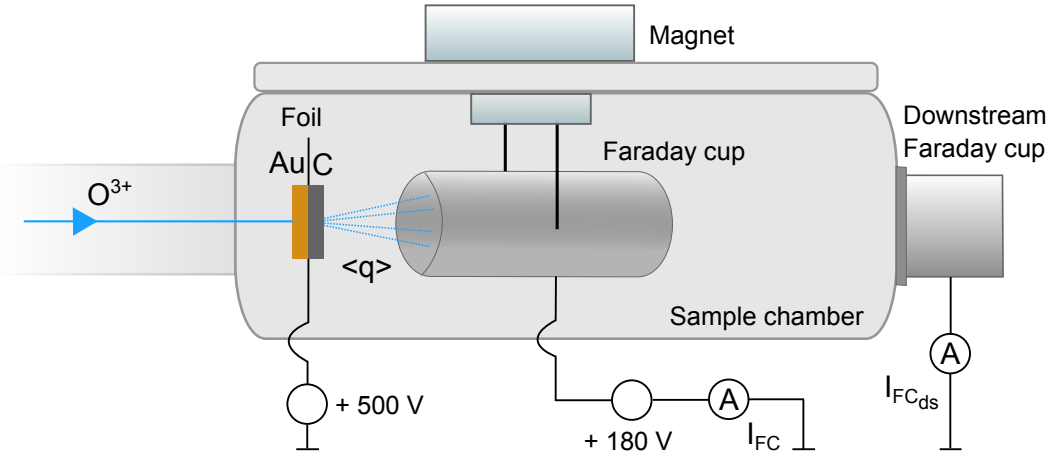

Figure 2.3: Schematic experimental setup for average charge state measurement.

The particle beam consisting of O^{3+} ions enters the sample chamber and hits the gold foil. While going through the foil the oxygen ions interact with the Au atoms. A positive voltage of +500 V is put on the foil in order to keep additional electrons that might be knocked out from the Au atoms in the foil. The carbon backing delivers more stability to the foil, as the gold layer is only several nanometers thick. Right after the foil the scattered ions go into a Faraday cup which is suspended from the lid of the sample chamber by means of a magnet. The Faraday cup is also isolated from the chamber and a positive voltage of +180 V is put on the cup to keep secondary electrons from escaping. The scattered oxygen ions fly into the cup and deliver their charge which can be measured as an electric current I_{FC} with an ampere meter.

In order to obtain the average charge state the electric current without going through the gold foil must be compared to the electric current when going

through the foil according to

$$< q >= \frac{I_{FC_{Au}}}{I_{FC}} \cdot 3 \tag{2.3}$$

where $< q >$ is the equilibrium charge state and I_{FC} is the current measured at the Faraday cup. The multiplication factor 3 comes from the fact that every oxygen ion that hits the gold foil has a positive triple charge (O^{3+}).

This procedure was carried out before every irradiation, especially when irradiating at different energies as the equilibrium charge state changes with the incident beam energy. For an incident beam energy of 4.6 MeV, which leads to 3.5 MeV on the YBCO surface, we measured $I_{FC} = 253$ nA without gold foil and $I_{FC_{Au}} = 440$ nA with gold foil. This calculates to $< q >= 5.2$ which agrees with theoretical values obtained through SRIM-TRIM simulations.

2.2.3 Sample Irradiation

Once the equilibrium charge state of the oxygen ions is determined the setup inside the sample chamber can be changed to the final setup for sample irradiation. Here we use a collimator with a diameter of 7.5 mm to focus the beam after the gold foil. This enables a nice and round beam spot on the sample ladder in the center of the chamber, see Fig. 2.4.

In order to calculate the irradiation time for the simulated target dose we need to first measure the current at the downstream Faraday cup. The exposure time can then be calculated with

$$t \cdot I_{FC} =< q > \cdot e \cdot A_{coll} \cdot D \tag{2.4}$$

where I_{FC} is the measured current at the downstream Faraday cup, $e = 1.6 \cdot 10^{-19}$ C, $A_{coll} = 0.44$ cm^2 is the area of the collimator and D is the target dose. With a measured current of $I_{FC} = 1$ μA the irradiation time for a target dose of $D = 10^{13}$ cm^{-2} is $t = 3$ s. Once the sample ladder with the mounted samples is put in place the beam is led into the chamber for the desired time by taking out an analyzing cup upstream in the beam line and which can be

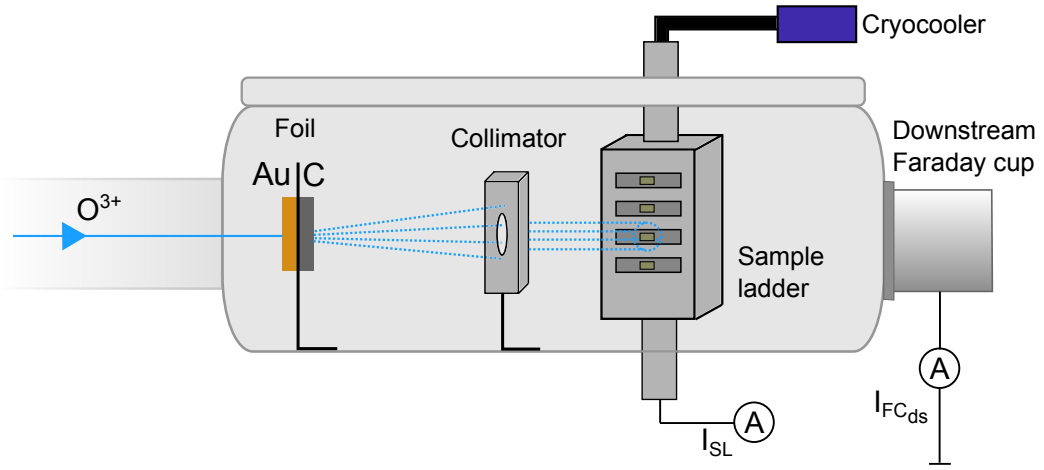

Figure 2.4: Schematic experimental setup for oxygen ion irradiation. Like the gold/carbon foil system, the collimator and sample ladder are turned by 90° into the oxygen beam.

put back in very fast to cut the beam. The sample ladder was initially cooled to -10 °C by a cryocooler to prevent excessive heating of the samples by the beam but as the irradiation periods for oxygen irradiation grew shorter the cooling system could be left out of the process in the end.

The chosen incident beam energy accounts for all losses caused by the foil system. For example, in order to achieve an oxygen beam of 3.5 MeV on the YBCO surface, see Fig. 1.3, the incident beam energy has to be set to 4.6 MeV. This was calculated through further SRIM-TRIM simulations that take the silver coating thickness, and the thickness of the gold/carbon foils into account. In the following chapters the chosen irradiation energies are the respective incident beam energies.

Chapter 3

Results and Discussion

Several YBCO samples were oxygen irradiated to different doses at three different energies. Magnetization measurements were conducted using a commercial SQUID-Magnetometer and from that the critical current density was calculated using the Bean model. Section 3.2 describes the results obtained for different irradiation energies. Furthermore the critical temperature was measured for each sample and the effect of oxygen irradiation is briefly discussed. Section 3.4 shows TEM images of a pristine and an irradiated sample and finally an annealing study is shown which was conducted in order to investigate the stability of the irradiation induced defects.

3.1 Magnetization Hysteresis

Each sample is fully characterized before and after irradiation in a commercial SQUID-Magnetometer (MPMS2, Quantum Design). MT-curves and magnetization hysteresis at temperatures near boiling points of various gases are recorded, namely at $T = 5$ K (liquid helium), $T = 27$ K (liquid neon), $T = 77$ K (liquid nitrogen) and at $T = 45$ K. The measurement procedure is always the same: the sample is fixed on a small glass plate using vacuum grease, that is horizontally inserted into a small slit in the center of a plastic straw. This straw is attached to the sample rod and inserted into the SQUID-Magnetometer. Figure 3.1 shows an example of two measurements, before and after oxygen irradiation at 4.6 MeV (3.5 MeV on the YBCO surface).

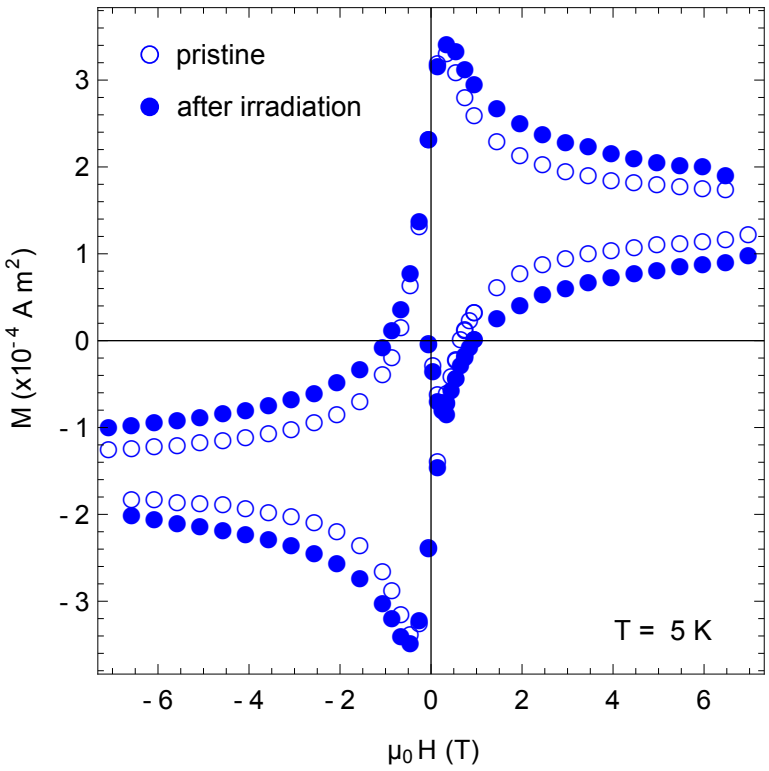

Figure 3.1: Magnetization hysteresis measured with the SQUID-Magnetometer for a pristine tape (empty circles) and after one second irradiation to an oxygen dose of $0.33 \cdot 10^{13}$ cm^{-2} (filled circles). The width of the hysteresis loop is almost doubled in high fields after irradiation.

Once the measurement system is stable at the desired temperature, the sample is transported through the coil system and the magnetic moment is recorded for different magnetic fields. Here the magnet is charged from 0 T to +7 T, then from +7 T to -7 T and finally from -7 T to +1 T in order to reconnect the hysteresis loop. As can be seen in Fig. 3.1 the hysteresis loop becomes wider after oxygen irradiation, where ΔM is almost doubled at 5 K in high fields after 4.6 MeV oxygen irradiation. The sample shown here was only exposed to the oxygen beam for 1 second to a dose of $0.33 \cdot 10^{13}$ cm^{-2}. The asymmetry of the magnetization hysteresis loop with respect to the field axis is a consequence of the ferromagnetic nature of the RABiTS substrate, which can be neglected as only the relative improvement is of interest.

At low fields, all vortices are assumed strongly pinned by the already existing rare earth nanoparticles and the irradiation induced defects do not contribute to additional vortex pinning here. With increasing field the irradiation in-

duced defects could effectively pin interstitial vortices, therefore explaining the observed enhancement in high fields.

The hysteresis loops at 27 K show a similar enhancement after oxygen irradiation in high fields, as can be seen in Fig. 3.2 on the left side. At this temperature similar results as from previous proton irradiation [16] are obtained but with irradiation time reduced to the order of a second instead of hours. The graph on the right side shows measurements at 45 K, where the signal is visibly smaller. Even at that temperature a slight enhancement after irradiation is still visible.

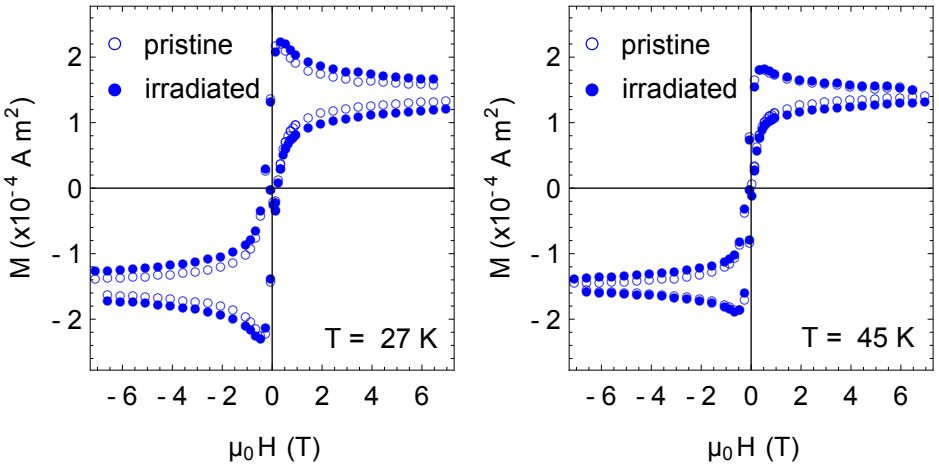

Figure 3.2: Magnetization hysteresis at 27 K and 45 K. At both temperatures improvement after irradiation is still visible.

At 77 K however only the ferromagnetic signal from the RABiTS substrate remains but for a small magnetization hysteresis in very low fields, see Fig. 3.3. The inset shows the low field region where we can see that ΔM stays the same before and after irradiation. The small change in the ferromagnetic signal was not observed in other samples and could stem from the uncertainty of the SQUID measurement or slight variation of the sample position and orientation in the plastic straw. Since only the width of the respective hysteresis loops is of interest the ferromagnetic signal and its change can be disregarded. No improvement has been made through post production particle irradiation so far at 77 K which is also consistent with earlier results on proton irradiated coated conductors.

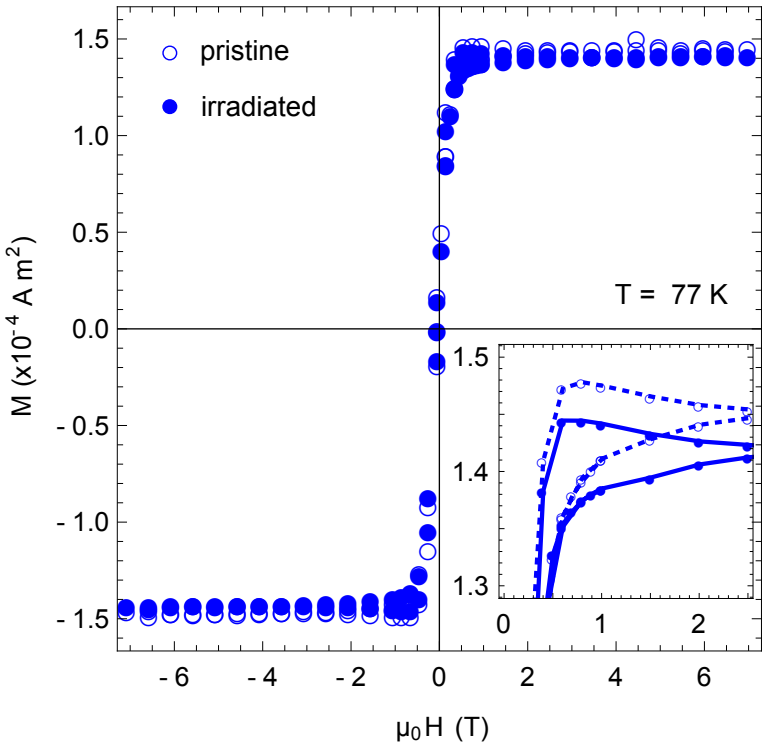

Figure 3.3: Magnetization hysteresis measured with the SQUID-Magnetometer at 77 K where the ferromagnetic background signal from the RABiTS substrate dominates. The inset shows a small part of the hysteresis loop in the low field region which has the same width before an after irradiation, thus no improvement can be detected.

3.2 Critical Current Density

From magnetization hysteresis we can calculate the critical current density J_c using the Bean model, as introduced in Chap. 1.2. We use a modified version of Equation 1.2, namely

$$J_c = \frac{2 \cdot \Delta M}{b(1 - \frac{b}{3a})} \tag{3.1}$$

where $M = \frac{m}{V}$ is the magnetization and ΔM is therefore the difference in magnetization at increasing and decreasing field in the hysteresis loop. The sample volume $V = abc$ is determined through the dimensions $a = b = 1.5$ mm

and $c = 1.2$ μm. The values of the magnetic moment m can be extracted directly from the SQUID data file by means of a python script where J_c is calculated for all temperatures.

3.2.1 Enhancement for 4.6 MeV Irradiation

Since J_c is proportional to ΔM, the critical current density increases with the width of the hysteresis loop. For the sample that was oxygen irradiated at 4.6 MeV to a dose of $0.33 \cdot 10^{13}$ cm^{-2} in just one second, the field dependence of J_c is shown in a double logarithmic plot in Fig. 3.4 for measurements at 5 K and at 27 K.

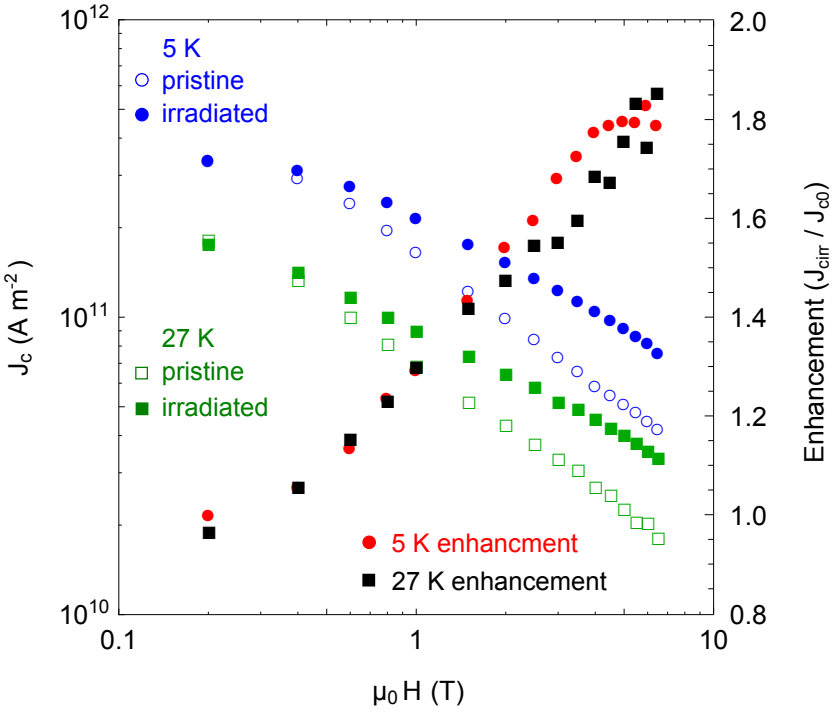

Figure 3.4: Magnetic field dependence of the critical current density at 5 K (blue) and 27 K (green), for an oxygen dose of $0.33 \cdot 10^{13}$ cm^{-2}. The J_c enhancement can be seen on the right side in red and black for the two temperatures respectively.

At 5 K and low magnetic field (0.2 T) $J_c = 2.5 \cdot 10^{11}$ A m^{-2} before and after irradiation. In the field range of 1 T - 6 T J_c is well described by the relation

$J_c \sim H^{-\alpha}$. Reported values of the exponent α depend strongly on the sample architecture and microstructure, for MOD-grown films α-values are typically in the range of 0.6 - 0.7 [22]. By overlaying the data points with a linear fit function the slope can be determined to $\alpha = 0.73$ in the pristine case, which is in good agreement with literature values. At 6 T the value of J_c has fallen to $4 \cdot 10^{10}$ A m^{-2}. After oxygen irradiation the critical current density starts out at the same value at 0.2 T. With increasing field the linear decrease of J_c progresses with a lower inclination where $\alpha = 0.53$, therefore nearly doubling J_c at high fields. This enhancement can be observed in Fig. 3.4 on the right side as the red curve for 5 K and the black curve for 27 K. This shows that also at 27 K we see a similar relative enhancement of J_c in high fields after oxygen irradiation. Here the major effect of irradiation is the reduction of the field-dependence of J_c, i.e. the reduction of α.

In order to find the optimum irradiation dose several samples were irradiated under same conditions at the same energy of 4.6 MeV for different time periods. The dose dependence of J_c after oxygen irradiation at 5 K is presented in Fig. 3.5.

The different colors represent the enhancement at magnetic fields of 0.2, 1, 2, 3 and 6 T. At the lowest field the maximum improvement is already reached at the lowest dose of $0.33 \cdot 10^{13}$ cm^{-2}, at all higher doses we can only see suppression. This means that J_c after irradiation is smaller in low fields, where the irradiation induced defects don't add to additional vortex pinning and moreover, they seem to weaken the successful pinning from the pristine structure. Similar behavior was observed in neutron irradiated coated conductors, where it is suggested, that the grain boundary network is responsible for this effect [23]. In all higher fields however the optimum is reached at a dose of $0.66 \cdot 10^{13}$ cm^{-2}, which would equal a irradiation time of 2 seconds with a beam current of 1 μA. For a magnetic field of 6 T J_c here is even more than doubled.

The rapid reduction of α with irradiation dose from 0.73 in the pristine sample to about 0.5 at optimal dose and down to 0.4 for over optimal dose is illustrated in Fig. 3.6 at 5 K and 27 K. With increasing field, J_c is expected to initially vary approximately as $H^{-1/2}$ and, when interstitial vortices appear, as H^{-1} [24]. The data here roughly follows this trend, although in the pristine case α only reaches a value of about 0.7.

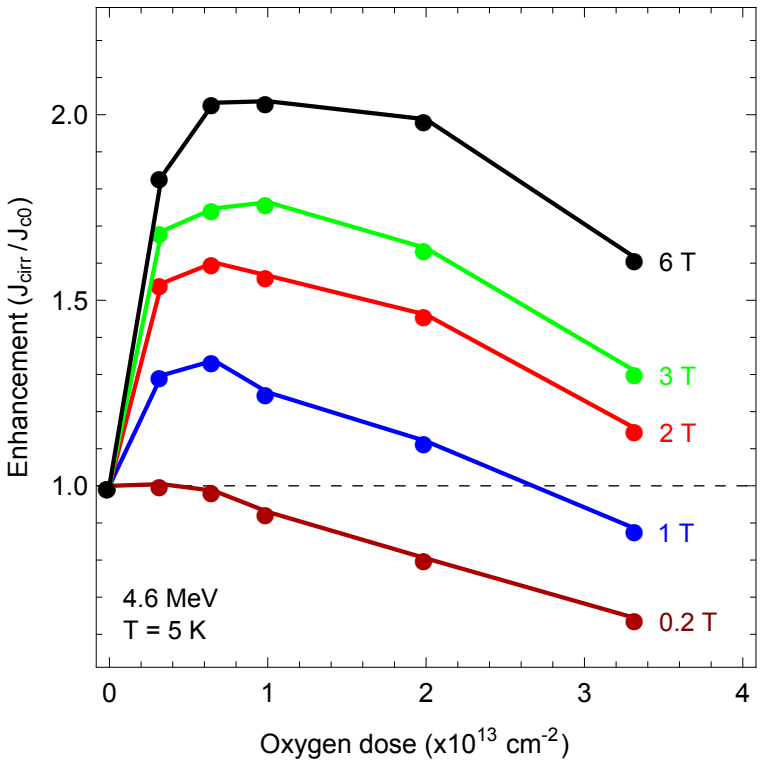

Figure 3.5: Irradiation dose dependence of the J_c enhancement at 5 K in fields of 0.2, 1, 2, 3 and 6 T. Each color represents the enhancement at a different magnetic field.

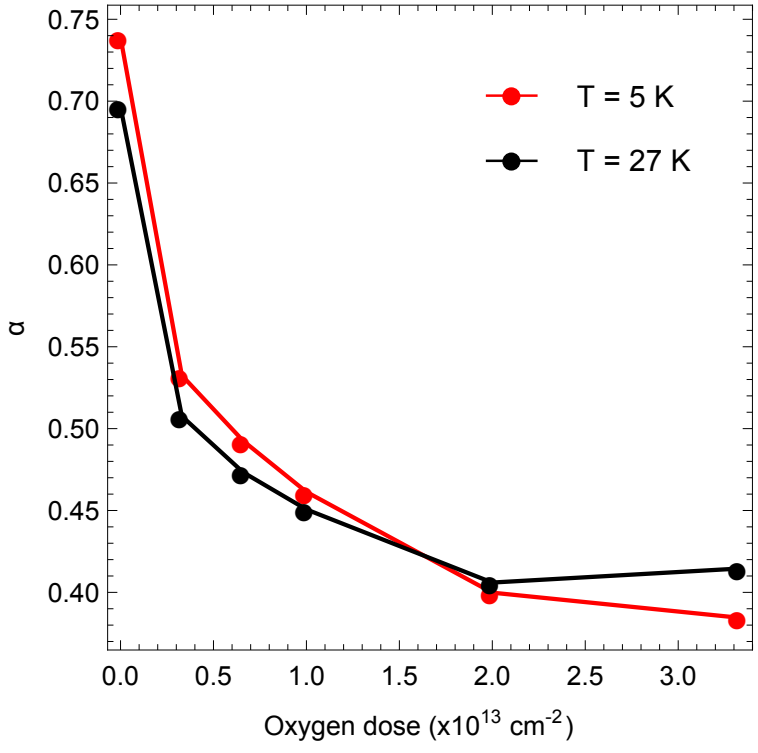

Figure 3.6: Dose dependence of the exponent α for 4.6 MeV oxygen irradiation.

At higher temperatures the optimum irradiation dose is reached even faster, as can be seen in Fig. 3.7. At 27 K the optimum is at a dose of $0.66 \cdot 10^{13}$ cm^{-2} only for fields higher than 1 T and the enhancement decreases faster with irradiation dose. At low fields no enhancement could be found for any of the doses.

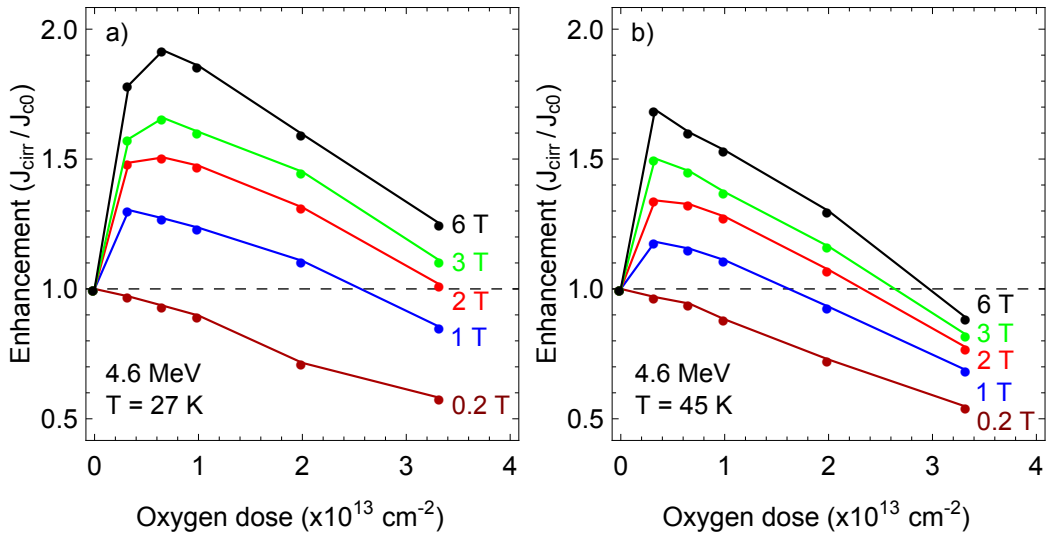

Figure 3.7: J_c enhancement at different fields at 27 K (a) and 45 K (b) for various oxygen irradiation doses.

At 45 K the optimum dose is at $0.33 \cdot 10^{13}$ cm^{-2} for all fields and at the highest dose of $3.3 \cdot 10^{13}$ cm^{-2} we found suppression of J_c for all fields. For the lowest dose presented here it was possible for the first time to actually still see enhancement at that high temperature. In high fields J_c is still improved by a factor of 1.7 which is similar to the observed enhancement at lower temperatures.

All the dose dependence data presented above show a striking asymmetry in which the enhancement of J_c rises rapidly at small doses, passes through the optimum, and then decreases gradually at high doses. This is beneficial for industrial application of the irradiation process since more than 80 % of the enhancement is already obtained for $0.33 \cdot 10^{13}$ cm^{-2} and therefore irradiation within one second. The results presented in this chapter have also been published in [18].

3.2.2 Comparison with other Irradiation Energies

In order to find the optimum irradiation energy we chose three different energies close together where the peak of maximum damage is still in the YBCO superconducting layer, i.e. 4 MeV, 4.6 MeV and 5 MeV. At 4.6 MeV the energy peak is more or less in the center of the YBCO layer, as can be seen in Fig. 1.3 (3.5 MeV on the sample). We also tried sample irradiation at 5 MeV ($\sim$ 4 MeV on the YBCO surface) for two different doses, where the peak is slightly shifted towards the substrate.

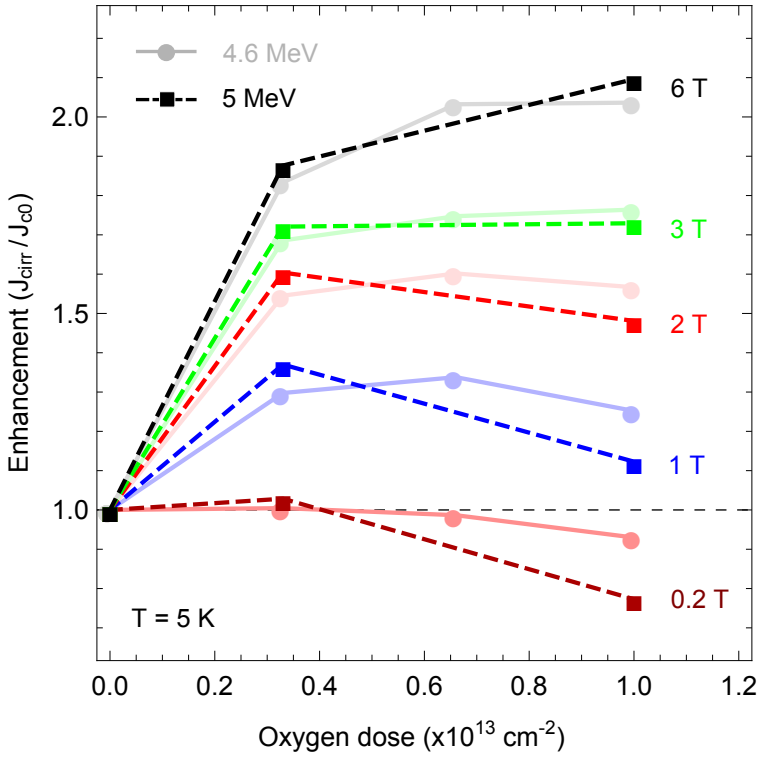

Figure 3.8: Comparison of the J_c enhancement at two different irradiation doses for 5 MeV and 4.6 MeV incident beam energy. At the lower dose the 5 MeV irradiation performs slightly better whereas 4.6 MeV irradiation shows more enhancement at the higher dose.

Figure 3.8 compares the enhancement at 5 K of the two different oxygen doses at 4.6 MeV and 5 MeV. For the lowest dose of $0.33 \cdot 10^{13}$ cm^{-2} irradiation at 5 MeV shows slightly more enhancement at all fields, while for the higher dose $1 \cdot 10^{13}$ cm^{-2} only high fields show increased enhancement at 5 MeV. However the doses at different energies compared here correspond to four different samples, therefore the small differences in enhancement at very low doses are

most likely due to the uncertainty of beam exposure time. Magnetization measurements at 27 K and 45 K show similar behavior, that is, slightly more enhancement at the low dose but less enhancement at the higher dose.

In order to check the J_c enhancement also for a lower irradiation energy, two samples were irradiated at 4 MeV ($\sim$ 3 MeV on the YBCO surface) to a dose of $0.33 \cdot 10^{13}$ cm^{-2} and $0.66 \cdot 10^{13}$ cm^{-2}, as can be seen in Fig. 3.9. Here, more enhancement can be only observed in low fields of 0.2 T, also at 27 K and 45 K (not shown). For all other fields however this lower energy shows no improvement as compared to irradiation at 4.6 MeV at dose $0.33 \cdot 10^{13}$ cm^{-2} and the difference is even bigger at a dose of $0.66 \cdot 10^{13}$ cm^{-2}. Here the enhancement factor for a field of 6 T falls from 2 to 1.6. Even though the energy difference to the optimal incident beam energy is very small, the effect observed can be interpreted by considering Fig. 1.3. With only 3 MeV on the sample surface almost half of the YBCO layer stays free of irradiation induced defects that are important for vortex pinning in higher applied fields.

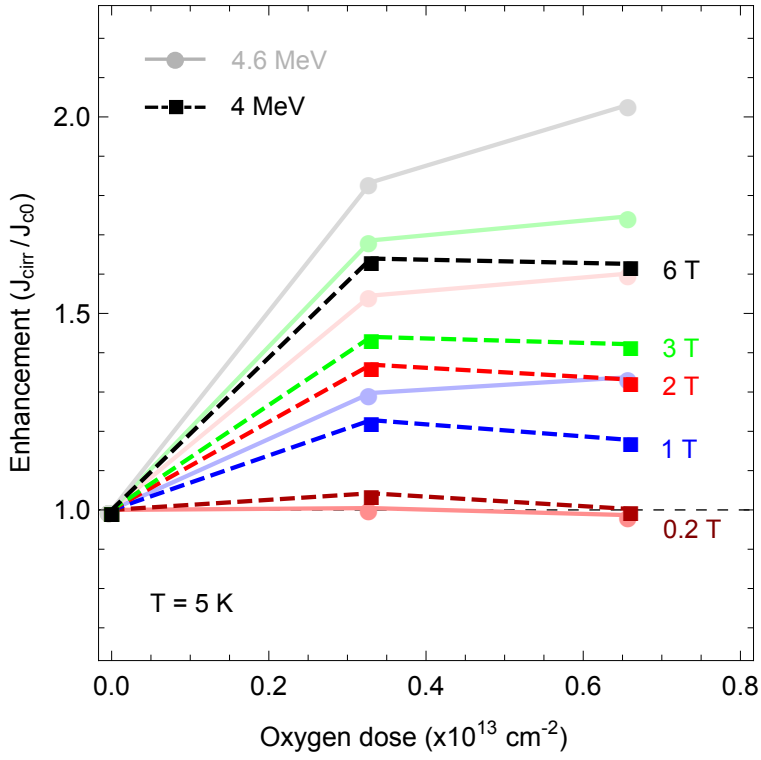

Figure 3.9: Comparison of the J_c enhancement at two different irradiation doses for 4 MeV and 4.6 MeV incident beam energy. The 4 MeV irradiation only shows better enhancement at low fields of 0.2 T, for all other fields is hows no improvement as compared to 4.6 MeV irradiation.

3.2.3 Comparison with "Straight Shot" Irradiation

All samples are irradiated using a gold foil with carbon backing in order to spread the beam and obtain a uniform beam spot, as described in Chap. 2.2.3. To demonstrate what would happen if samples are irradiated without using the gold foil the incident beam energy was reduced to 3.5 MeV. According to SRIM-TRIM calculations, that is the energy reaching the YBCO layer without the foil system. Figure 3.10 shows a comparison of three different samples irradiated for one second as a bar chart. The y-axis gives the J_c enhancement after irradiation and the x-axis shows five different applied magnetic fields. In blue and green we see again the comparison between irradiation at 5 MeV and 4.6 MeV, as already demonstrated in Fig. 3.8. The red bars show the J_c enhancement of a sample irradiated at 3.5 MeV without the gold/carbon foil system, thus "straight shot" irradiation. The straight shot irradiation shows no improvement as compared to the other two samples and has less enhancement at all applied fields.

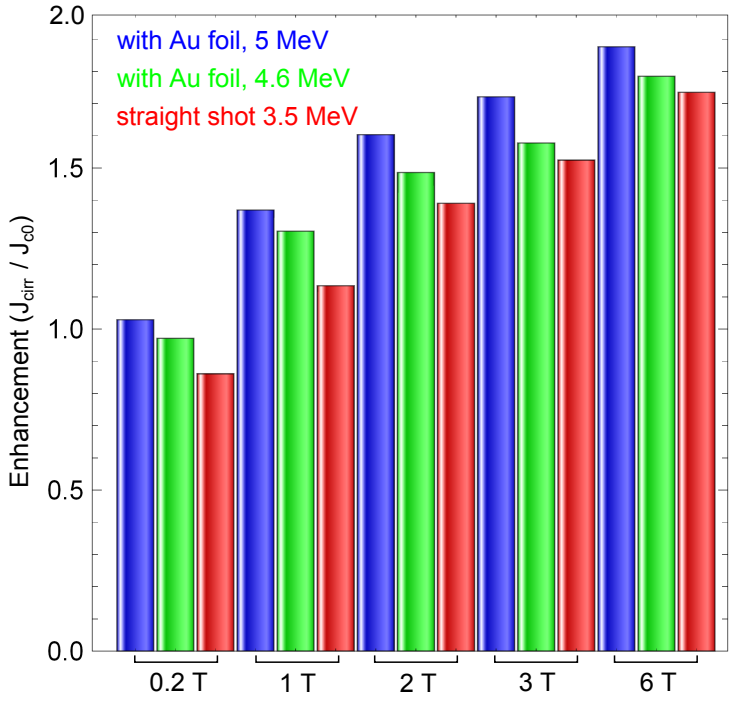

Figure 3.10: Comparison of the J_c enhancement of three different samples all irradiated for 1 second or a dose of $0.33{\cdot}10^{13}$ cm^{-2}. Irradiation without the gold/carbon foil system with 3.5 MeV (red bars) shows no improvement as compared to 4.6 MeV (green) and 5 MeV (blue) irradiation.

Before every sample irradiation a "picture" of the beam spot is taken by means of a radiographic film. A small strip of the film is placed in the beam line and exposed to the beam as short as possible, usually less than a second. At the area where the ion beam hits the film it turns darker. When going through the gold/carbon foil we can see a round and uniform beam spot with the diameter of the collimator. However by taking a "picture" of the straight shot without foil we see that the beam spot is smaller ($\sim 5 - 10$ mm diameter) and has hot spots in the center, as can be seen in Fig. 3.11.

Figure 3.11: Picture of the beam spot on a radiographic film without the gold/carbon foil system. The beam spot is smaller, has no perfect circular shape and shows hot spots in the center. The orange color indicates that the film was heated over 50 °C in less than a second.

The orange color in the center of the beam spot indicates that the film was exposed to more than +50 °C, i.e. the film starts to burn in less than a second. As we don't want the samples to be exposed to such heat and non uniform irradiation this shows that the use of the foil system is of interest in order to obtain steady and reliable results.

3.3 Critical Temperature

With the SQUID-Magnetometer it is also possible to measure the critical temperature T_c of each sample as part of the full characterization process. For this we use the zero field cooling method, where the SQUID-Magnetometer is cooled to 75 K with no applied magnetic field. When the temperature is stable, the magnet is charged to $2 \cdot 10^{-3}$ T and with that constant magnetic field the temperature is scanned in small steps up to 95 K and the magnetic moment is recorded for each temperature point. For the pristine sample, which is represented by the black curve in Fig. 3.12, we find $T_c = 90$ K. The MT curve is normalized in order to be able to compare to MT curves of other samples.

In accordance with the standard procedure for magnetization measurements, T_c is taken at 90% of the transition and the transition width ΔT_c is defined as the region between 10% and 90% of the transition. For the pristine sample $\Delta T_c = 3$ K, measurements of all the pristine samples involved in the irradiation experiments show that T_c and ΔT_c is constant throughout the samples (not shown here).

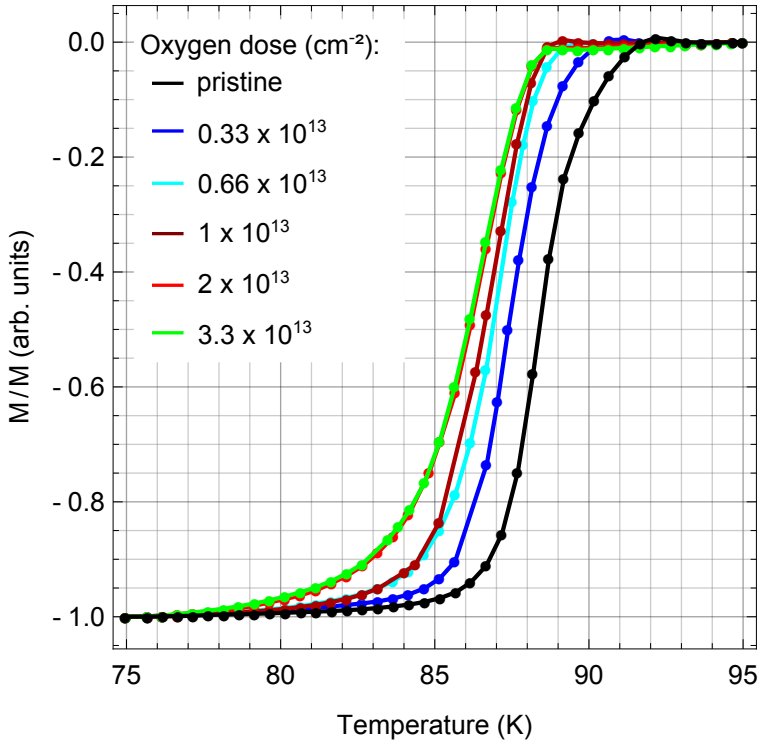

Figure 3.12: Effect of different oxygen irradiation doses on the critical temperature.

Figure 3.12 shows the effect of the different oxygen irradiation doses from above on the critical temperature. As expected T_c is suppressed after irradiation and the higher the irradiation dose, the more T_c is suppressed. This is a common effect for irradiated superconductors as the irradiation causes changes of the chemical composition of the superconducting layer. For the one-second-irradiation to a dose of $0.33 \cdot 10^{13}$ cm^{-2} however the critical temperature is only suppressed by 1 K, for the highest dose T_c drops below 87 K and the transition becomes wider.

3.4 TEM Images

Diffraction contrast transmission electron microscopy (TEM) images of a pristine and a sample irradiated to an oxygen dose of $1 \cdot 10^{13}$ cm^{-2} were obtained by D. J. Miller and his team from the Electron Microscopy Center at the Center for Nanoscale Materials. The TEM image of the pristine sample, Fig. 3.13 (a), shows the expected defect structure of MOD coated conductors with rare earth oxide nanoparticles of a size of $20 - 50$ nm and a few stacking faults. Another TEM image taken after oxygen irradiation reveals a different defect structure, as can be seen in Fig. 3.13 (b). It can be demonstrated that oxygen irradiation produces a large number of small defects of approximately 5 nm in diameter (highlighted by the dashed white circles). For both images the c-axis is horizontal.

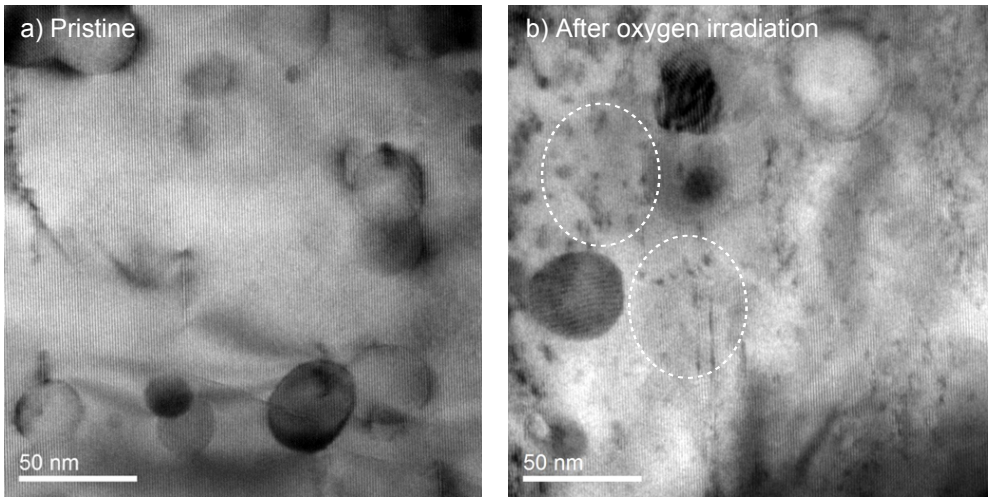

Figure 3.13: Diffraction contrast TEM images of pristine (a) and irradiated (b) samples. In the pristine samples, the TEM baseline structure shows large nanoparticles ($\sim$ 20–50 nm), stacking faults, and large defect-free regions, whereas in the irradiated samples small defects ~ 5 nm in diameter appear randomly distributed within the baseline structure as highlighted by the dashed white circles.

These images suggest a mixed pinning landscape composed of rare earth oxide nanoparticles, twin boundaries and irradiation induced point defects. The irradiation induced defects can be identified as the main source for increased vortex pinning.

3.5 Annealing

In order to investigate the stability of the irradiation induced defects an annealing study was conducted with two separate samples. One of the samples is pristine, the other was irradiated to an oxygen dose of $0.66 \cdot 10^{13}$ cm^{-2}. The samples were annealed in a commercial tube furnace in a dry air environment at constant pressure. For that, the tube furnace is first set to 450 °C for 30 minutes to burn out all possible contamination. Afterwards the furnace is set to the desired temperature and once T =const. is achieved the sample is inserted into the glass tube by means of a small glass shovel. Each sample is annealed for 60 minutes at T_A = 100, 200, 300, 350, 400, and 450 °C and after every annealing cycle the sample is fully characterized in the SQUID-Magnetometer. The following chapters describe changes observed in the critical temperature and the critical current density.

3.5.1 T_c Dependence with Annealing Temperature

Using the SQUID-Magnetometer magnetization versus temperature curves are recorded after every annealing step and then normalized in order to compare T_c after every measurement. After irradiation T_c is depressed by 2 K, as can be seen in Fig. 3.14 (a).

After annealing for T_A = 100 °C and T_A = 200 °C for an hour T_c recovers again towards the pristine value. At T_A = 300 °C T_c has fully recovered and at higher annealing temperatures it increases even further. We see a similar effect when annealing a pristine sample, see Fig. 3.14 (b). With the first two annealing cycles there is almost no change and the normalized T_c curves match. At higher annealing temperatures T_c increases again. This becomes also visible in Fig. 3.15, where the values of T_c of the pristine and irradiated sample are plotted against each annealing temperature. The inset shows the transition width which stays more or less constant for both samples until T_A = 400 °C. However after annealing at 450 °C the transition becomes wider for both samples, with this effect being stronger for the pristine sample.

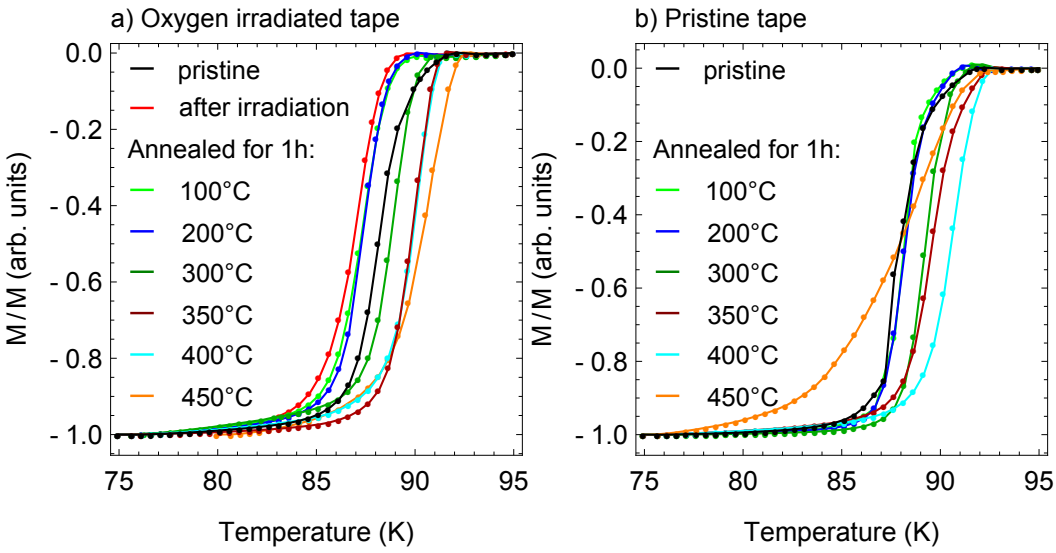

Figure 3.14: Normalized T_c curves for different annealing temperatures T_A for an oxygen irradiated (a) and a pristine sample (b).

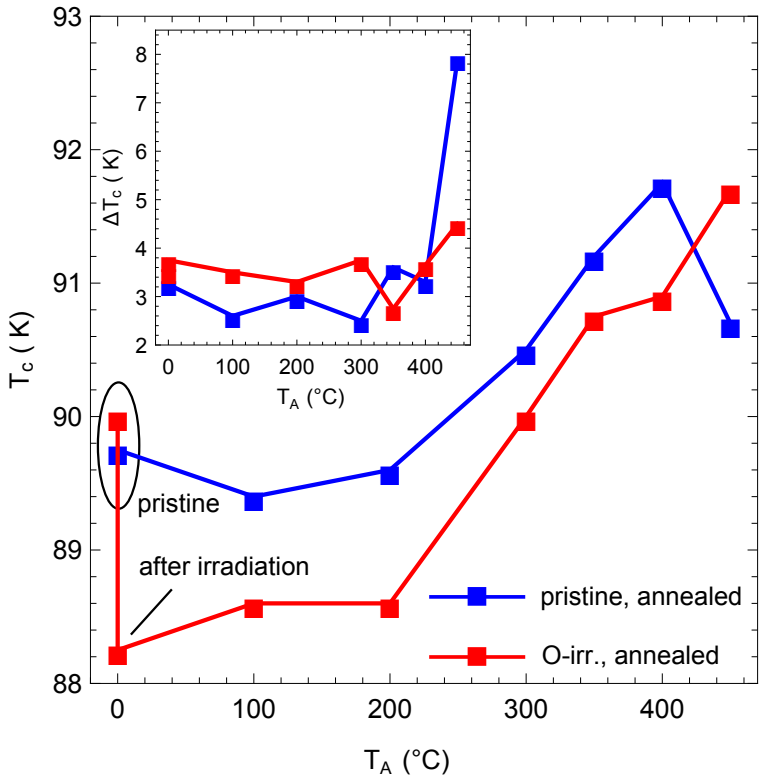

Figure 3.15: T_c values of the irradiated (red) and pristine (blue) sample in dependence of T_A. The value of T_c is taken at 90 % of the transition. The inset shows the transition width in dependence of annealing temperature.

There are several possible approaches to explain the increase of T_c with higher annealing temperatures. If we look at the oxygen content equilibrium of $YBa_2Cu_3O_{7-x}$ as a function of temperature and pressure we find that for a partial pressure of oxygen in air of 0.21 atm, x becomes bigger with increasing temperature [25, 26]. There is not much difference for temperatures up to $T_A = 300$ °C, but at higher temperatures the oxygen content in the sample can change and therefore influence T_c. Similar annealing experiments on YBCO coated conductors in pure oxygen show little to no increase of T_c at the same annealing temperatures [27]. This is to be expected as the samples undergo post-growth annealing at 450 °C in pure oxygen at AMSC. Since we anneal in dry air, we suspect to loose oxygen at higher temperatures, the increase of T_c could possibly point to overdoping by the manufacturer.

3.5.2 J_c Dependence with Annealing Temperature

The question that inspired this annealing experiment was to investigate the stability of the irradiation induced defects and if the sample could survive a possible quench. For that we looked at the J_c curves before irradiation, after irradiation and after every annealing cycle. Figure 3.16 (a) shows all these J_c curves at 5 K of a sample that was irradiated to an oxygen dose of $0.66 \cdot 10^{13}$ cm^{-2}. After irradiation J_c is doubled in high fields, as indicated by the dashed black line. After annealing at $T_A = 100$ °C and $T_A = 200$ °C for an hour each, there is not too much change in the J_c curve, we loose a bit in high fields but there is still a definite enhancement visible. This suggests that the irradiation induced defects are quite stable and the sample would withstand a quench.

After annealing at higher temperatures however J_c starts to be suppressed in low fields as well. In order to check if that effect is caused by the irradiation induced defects the same annealing cycle was performed with a pristine sample, see Fig. 3.16 (b). Here we can see the same effect as in the irradiated sample, not much change after the first two annealing cycles but suppression at all fields starting at $T_A = 300$ °C and higher. The inset shows the suppression of J_c at field 0.2 T for both samples depending on the annealing temperature.

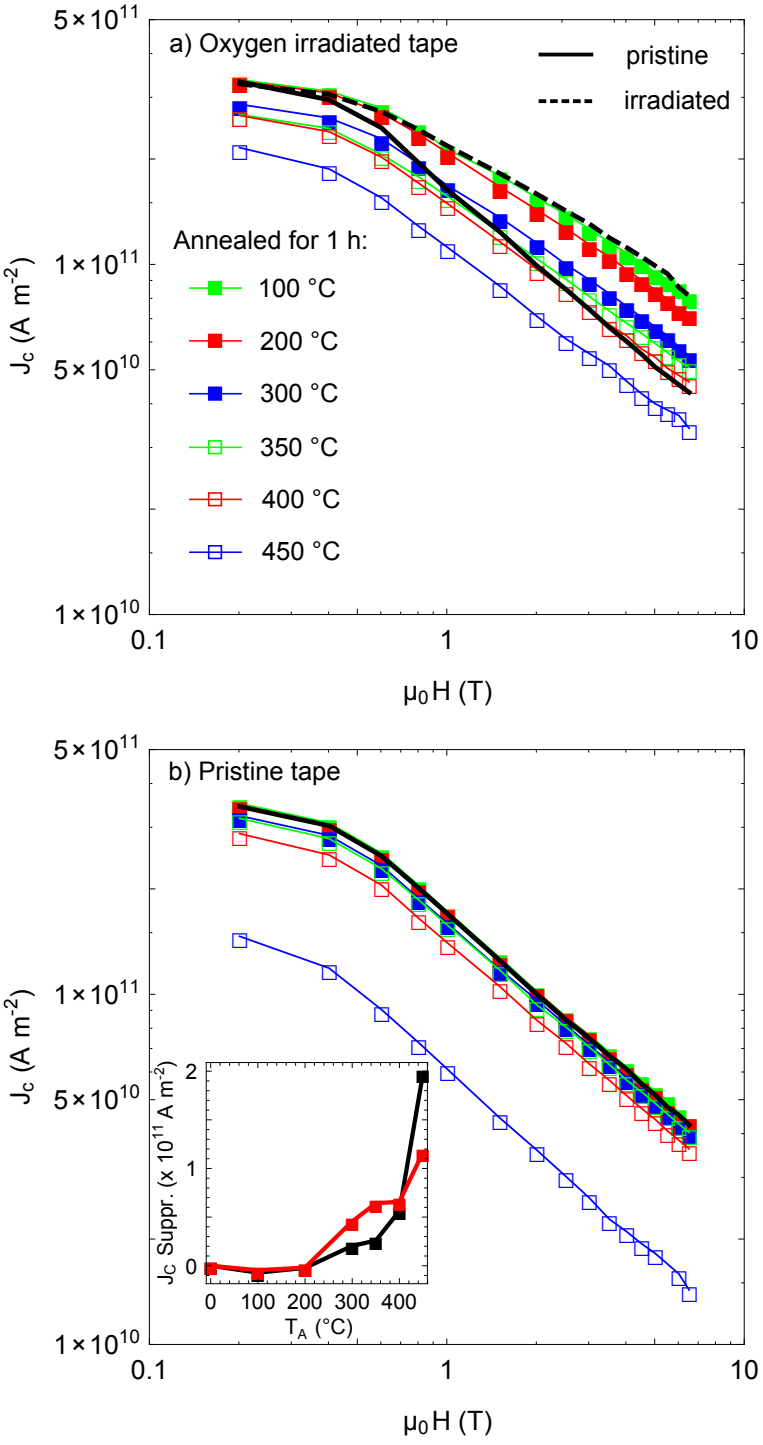

Figure 3.16: Critical current as a function of field for an oxygen irradiated (a) and a pristine sample (b) for different annealing temperatures at 5 K. For the irradiated sample J_c is doubled in high fields and starts decreasing again after every annealing cycle towards the pristine value. Starting at 300 °C J_c is also suppressed in low fields, the same effect is visible in the pristine sample that was annealed. The inset in (b) shows the suppression of J_c at field 0.2 T for both samples in dependence of T_A. After annealing at 450 °C both samples show J_c curves far below the pristine example.

As we can also see this effect in the pristine sample, it is safe to say that it is not caused by the oxygen irradiation but rather by possible rearrangement of nanoparticles in the as grown defect structure of the superconductor, or of the already mentioned change in oxygen content. For another possible explanation for the decrease of J_c we must consider grain boundaries. The effect of the grain boundary geometry on the value of J_c has been extensively studied [28,29]. The decrease of J_c can be interpreted as oxygen depletion from grain boundaries. This can lead to decreasing grain coupling and a consequent decrease of pinning of intergranular vortices.

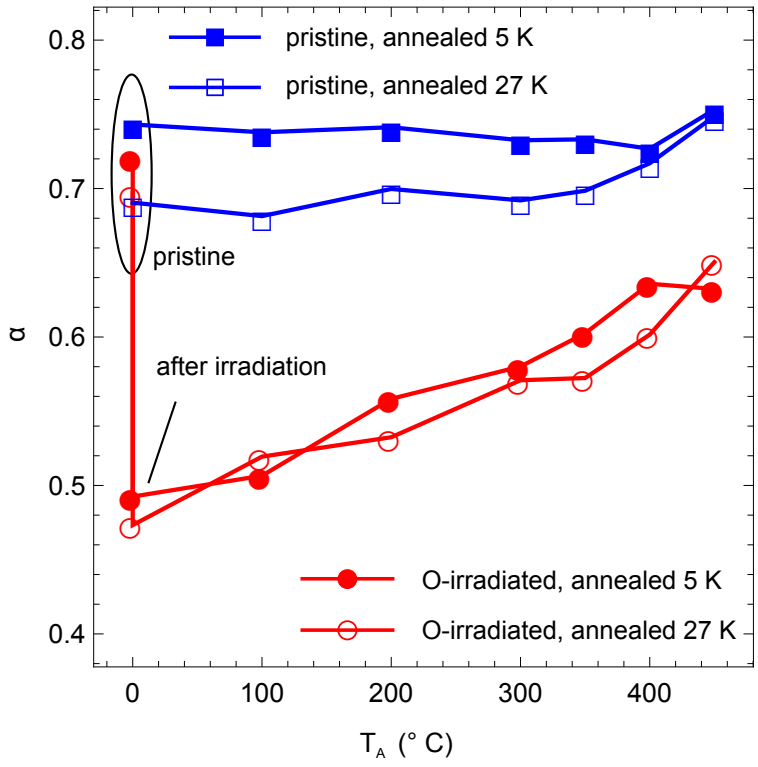

Figure 3.17: Evolution of α with annealing temperature at 5 K and 27 K for the pristine (blue) and oxygen irradiated sample (red). In the pristine case α stays constant throughout the annealing experiment whereas α is lower after irradiation and creeps back towards the pristine value with every annealing cycle.

Figure 3.17 shows the evolution of the α exponent for both annealed samples at 5 K and 27 K. For the pristine sample α stays constant at approximately 0.7 throughout all annealing cycles. Only after annealing at 450 °C we see a slight change in α which reflects the wider transition width and extreme drop

of J_c showed above. In the case of the oxygen irradiated sample $\alpha = 0.5$ after irradiation and with every annealing cycle α creeps back toward the pristine value. Values for 27 K are also shown here, to demonstrate that we see the same effect on J_c also at that temperature.

Diffraction contrast TEM images (not shown here) also reveal that the irradiation induced defects don't vanish but seem to rearrange in clusters and more defect free regions become visible. Images of the annealed sample seem to also exhibit more stacking faults than non annealed samples, it is possible however that these stacking faults also exist in the pristine sample but were not detected in the region investigated.

Conclusion and Outlook

The objective of this thesis was to demonstrate the enhancement of the critical current density J_c in high magnetic fields of state-of-the-art production-line $YBa_2Cu_3O_{7-x}$ coated conductors through particle irradiation. Square samples with dimensions of 1.5 mm x 1.5 mm were patterned using photolithography and Ar-ion milling at the Center for Nanoscale Materials at Argonne National Laboratory. The samples were irradiated using the 6.0-MV tandem Van de Graaff accelerator at Western Michigan University with $^{16}O^{3+}$ ions beams oriented along the normal of the film plane (c-axis). Magnetization hysteresis and measurements of the critical temperature were obtained by means of a commercial SQUID-Magnetometer before and after irradiation and J_c was calculated using Bean's critical state model.

Oxygen irradiation at different energies demonstrated the doubling of J_c in fields of 6 T at 5 K and 27 K, using a 3.5 MeV oxygen beam with an exposure time of the order of 1 s. Enhancement of J_c in high fields could also still be observed at 45 K, however at 77 K no improvement could be found. Transmission electron microscopy images reveal that the enhanced critical current is due to finely dispersed small clusters approximately 5 nm in diameter. These small clusters can be identified as the main source for increased vortex pinning. The major effect of the irradiation induced defects is the reduction of the field dependence of J_c, which can be attributed to the mixed pinning landscape composed of strong pre-existing pin sites and the finely dispersed irradiation induced defects. An annealing study shows that the J_c enhancement is stable up to $\sim$ 200 °C for over an hour and thus the enhanced sample should survive a quench.

The irradiation is made on production line samples through the protective silver coating and does not require any modification of the growth process. This

doubling of J_c within 1 s or less is now at the level required for an industrial reel-to-reel post-processing and opens a viable approach to address the challenge in HTS conductor development, namely, their reduced performance in even small applied magnetic fields. With the standard accelerator used for these experiments possibilities are open for even further enhancement using heavier ions such as chlorine or potassium.

Bibliography

[1] Committee on Opportunities in High Magnetic Field Science; Solid State Sciences Committee; Board on Physics & Astronomy; Division on Engineering & Physical Sciences; National Research Council. *Opportunities in High Magnetic Field Science*. The National Academies Press, Washington D.C., 2005.

[2] C. P. Bean. Magnetization of Hard Superconductors. *Physical Review Letters*, 8(6):250–253, 1962.

[3] C. P. Bean. Magnetization of High-Field Superconductors. *Reviews of Modern Physics*, 36:31–39, 1964.

[4] Y. B. Kim, C. F. Hempstead, and A. R. Strnad. Magnetization and Critical Supercurrents. *Physical Review*, 129(2):528–536, 1963.

[5] A. M. Campbell and J. E. Evetts. Critical Currents in Superconductors. *Advances in Physics*, 21(199), 1972.

[6] V. Selvamanickam, D. W. Hazelton, L. Motowidlo, F. Krahula, J. Hoehn, M. S. Walker, and P. Haldar. High-Temperature Superconductors for Electric Power and High-Energy Physics. *Journal of the Minerals Metals & Materials Society*, 50:27–30, 1998.

[7] A. P. Malozemoff. Second-Generation High-Temperature Superconductor Wires for the Electric Power Grid. *Annual Review of Materials Research*, 42:373–397, 2012.

[8] X. Obradors and T. Puig. Coated conductors for power applications: materials challenges. *Superconductor Science and Technology*, 27(4), 2014.

[9] J. Hua, U. Welp, A. Kayani, Z. L. Xiao, G. W. Crabtree, and W.-K. Kwok. Vortex pinning by compound defects in $YBa_2Cu_3O_{7-\delta}$. *Physical Review B*, 82(2), 2010.

[10] L. Civale, A. D. Marwick, T. K. Worthington, M. A. Kirk, J. R. Thompson, L. Krusin-Elbaum, Y. Sun, J. R. Clem, and F. Holtzberg. Vortex confinement by columnar defects in $YBa_2Cu_3O_7$ crystals: Enhanced pinning at high fields and temperatures. *Physical Review Letters*, 67(5), 1991.

[11] W.-K. Kwok, L. M. Paulius, V. M. Vinokur, A. M. Petrean, R. M. Ronningen, and G. W. Crabtree. Anisotropically splayed and columnar defects in untwinned $YBa_2Cu_3O_{7-\delta}$. *Physical Review B*, 58(21), 1998.

[12] Yimei Zhu, Z. X. Cai, R. C. Budhani, M. Suenaga, and D. O. Welch. Structures and effects of radiation damage in cuprate superconductors irradiated with several-hundred-mev heavy ions. *Physical Review B*, 48(9), 1993.

[13] L. Fang, Y. Jia, V. Mishra, C. Chaparro, V. K. Vlasko-Vlasov, A. E. Koshelev, U. Welp, G. W. Crabtree, S. Zhu, N. D. Zhigadlo, J. Karpinski, and W.-K. Kwok. Huge critical current density and tailored superconducting anisotropy in $SmFeAsO_{0.8}F_{0.15}$ by low-density columnar-defect incorporation. *Nature Communications*, 4, 2013.

[14] T. Tamegai, T. Taen, H. Yagyuda, Y. Tsuchiya, S. Mohan, T. Taniguchi, Y. Nakajima, S. Okayasu, M. Sasase, and H. Kitamura. Effects of particle irradiations on vortex states in iron-based superconductors. *Superconductor Science and Technology*, 25(8), 2012.

[15] H. Matsui, H. Ogiso, H. Yamasaki, T. Kumagai, M. Sohma, I. Yamaguchi, and T. Manabe. 4-fold enhancement in the critical current density of $YBa_2Cu_3O_7$ films by practical ion irradiation. *Applied Physics Letters*, 101(23), 2012.

[16] Y. Jia, M. Leroux, D. J. Miller, J. G. Wen, W.-K. Kwok, U. Welp, M. W. Rupich, X. Li, S. Sathyamurthy, S. Fleshler, A. P. Malozemoff, A. Kayani, O. Ayala-Valenzuela, and L. Civale. Doubling the critical current density

of high temperature superconducting coated conductors through proton irradiation. *Applied Physics Letters*, 103, 2013.

[17] James F. Ziegler, Jochen P. Biersack, and Matthias D. Ziegler. *The Stopping and Range of Ions in Matter*. Lulu Press Co., 15th edition, 2015.

[18] M. Leroux, K. J. Kihlstrom, S. Holleis, M. W. Rupich, S. Sathyamurthy, S. Fleshler, H. P. Sheng, D. J. Miller, S. Eley, L. Civale, A. Kayani, P. M. Niraula, U. Welp, and W.-K. Kwok. Rapid doubling of the critical current of $YBa_2Cu_3O_{7-\delta}$ coated conductors for viable high-speed industrial processing. *Applied Physics Letters*, 107, 2015.

[19] Martin W. Rupich, Darren T. Verebelyi, Wei Zhang, Thomas Kodenkandath, and Xiaoping Li. Metalorganic Deposition of YBCO Films for Second-Generation High-Temperature Superconductor Wires. *MRS Bulletin*, 29:572–578, 2004.

[20] J. A. Xia, N. J. Long, N. M. Strickland, P. Hoefakker, E. F. Talantsev, X. Li, W. Zhang, T. Kodenkandath, Y. Huang, and M. W. Rupich. TEM observation of the microstructure of metal-organic deposited YBaCuO with Dy additions. *Superconductor Science and Technology*, 20:880–885, 2007.

[21] M. Mayer. American Institute of Physics Conference Proceedings. *SIMNRA, a Simulation Program for the Analysis of NRA, RBS and ERDA*, volume 475, 1999.

[22] M. Miura, B. Maiorov, S. A. Baily, N. Haberkorn, J. O. Willis, K. Marken, T. Izumi, Y. Shiohara, and L. Civale. Mixed pinning landscape in nanoparticle-introduced $YGdBa_2Cu_3O_y$ films grown by metal organic deposition. *Physical Review B*, 82(18), 2011.

[23] M. Eisterer, R. Fuger, R. Chudy, F. Hengstberger, and H. W. Weber. Neutron irradiation of coated conductors. *Superconductor Science and Technology*, 23, 2010.

[24] A. E. Koshelev and A. B. Kolton. Theory and simulations on strong pinning of vortex lines by nanoparticles. *Physical Review B*, 84(10), 2011.

[25] Jun-ichi Shimoyama, Shigeru Horii, Kenji Otzschi, and Kohji Kishio. How to Optimize Critical Current Performance of RE123 Materials by Controlling Oxygen Content. *MRS Proceedings*, 689, 2002.

[26] J. D. Jorgensen, B. W. Veal, A. P. Paulikas, L. J. Nowicki, G. W. Crabtree, H. Claus, and W.-K. Kwok. Structural properties of oxygen-deficient $YBa_2Cu_3O_{7-\delta}$. *Physical Review B*, 41(4), 1990.

[27] S. Eley, M. Leroux, M. W. Rupich, D. J. Miller, H. Sheng, P. M. Niraula, A. Kayani, U. Welp, W.-K. Kwok, and L. Civale. Decoupling and tuning competing effects of different types on flux creep in irradiated $YBa_2Cu_3O_{7-\delta}$ ccoated conductors. arXiv:1602.04344, 2016.

[28] D. Matthew Feldmann, Terry G. Holesinger, Ron Feenstra, and David C. Larbalestier. A Review of the Influence of Grain Boundary Geometry on the Electromagnetic Properties of Polycristalline $YBa_2Cu_3O_{7-x}$ Films. *Journal of the American Ceramic Society*, 91(6):1869–1882, 2008.

[29] H. Hilgenkamp and J. Mannhart. Grain boundaries in high-T_c superconductors. *Reviews of M*, 74(2):485–549, 2002.

List of Figures